ChemComm

COMMUNICATION

View Article Online
View Journal | View Issue

Cite this: *Chem. Commun.*, 2024, **60**, 12710

Received 30th July 2024,
Accepted 3rd October 2024

DOI: 10.1039/d4cc03845b

rsc.li/chemcomm

Hydroxylation boosted low-overpotential CO_2 reduction to ethylene for a Cu/PTFE electrode†

Yifeng Wang,[ab] Haoliang Huang,[ac] Shengjie Zhang,[a] Hao Zhang,[a] Chao Jing, *[ab] Jian-Qiang Wang *[ab] and Linjuan Zhang *[ab]

We present a Cu/PTFE electrode for the CO_2 reduction reaction with a high coverage of *OH which facilitates both the activation of CO_2 and the C–C coupling, leading to a faradaic efficiency for ethylene exceeding 50% at an exceptionally low potential of −246 mV *vs.* RHE, with the maximum $FE_{C_2H_4}$ reaching 60.3%.

The escalating global levels of CO_2 and the excessive consumption of fossil fuels present major obstacles to sustainable development.[1–3] The CO_2 reduction reaction (CO_2RR), powered by renewable energy, emerges as a viable solution for CO_2 conversion while generating high-value chemicals under ambient conditions. Among various products of the electrochemical CO_2RR, multi-carbon compounds, especially ethylene, have garnered significant attention due to their versatility in industry.[4–6] Cu is the only single-metal catalyst capable of reducing CO_2 to diverse multi-carbon compounds, owing to the appropriate adsorption energy for *CO and *H species.[7,8] Cu-based catalysts are thus extensively employed in the CO_2RR to produce ethylene; however, there are still challenges including high overpotentials,[9,10] limited ethylene selectivity,[11,12] and competing hydrogen evolution reactions.[13,14]

Among Cu-based catalysts, $Cu(OH)_2$ exhibits notable selectivity towards the production of ethylene in the CO_2RR, attributed to the high *OH coverage on the Cu surface derived from $Cu(OH)_2$ during the CO_2RR process.[15,16] The presence of *OH promotes the adsorption of CO at an atop site ($*CO_{atop}$) on Cu rather than at a bridge site ($*CO_{bridge}$)[17] and impacts the work function of the Cu surface,[18] which facilitates the C–C coupling to generate C_{2+} products. Many efforts have been made to further enhance the ethylene selectivity of $Cu(OH)_2$ catalysts, including morphology and facet engineering,[19,20] tuning surface *OH amounts and particle size[15,18] and microenvironment control.[21] Polytetrafluoroethylene (PTFE) has been used to suppress the hydrogen evolution side reaction by enhancing the local hydrophobic environment of the catalyst and augmenting the solid–liquid–gas interfaces, which effectively enhances the selectivity for C_2H_4.[14,21] In addition to the selectivity, the overpotential for the CO_2RR stands as a pivotal merit for evaluating electrocatalytic performance. For most CO_2RR catalysts, the overpotentials required for achieving high selectivity (over 50%) of ethylene typically exceed 500 mV.[10,22,23] These high overpotentials are commonly attributed to the significant energy barriers associated with the first step of CO_2 activation and the step of carbon–carbon coupling. Achieving both high ethylene selectivity and low overpotentials remains a significant challenge in the realm of CO_2RR.

In this study, to enhance the active sites and catalytic ability, an ion sputtering method was employed to deposit nano-sized Cu catalysts onto the PTFE membrane, to obtain a uniformly dispersed Cu/PTFE electrode with good hydrophobicity and sufficient mechanical strength (Fig. S1 and S2, ESI†). Furthermore, to modulate the surface *OH, Cu particles were sputtered under dry and moist Ar atmospheres, denoted as D_Cu and M_Cu, respectively. The moist atmosphere was achieved by introducing water molecules through the addition of a hygroscopic polylactide (PLA) material into the vacuum chamber of the ion sputtering coater, which facilitated the formation of $Cu(OH)_2$ (Fig. 1a and Fig. S3, ESI†). Experimental results demonstrated that our M_Cu catalyst exhibited high selectivity and low overpotential for the generation of ethylene, with a faradaic efficiency for ethylene ($FE_{C_2H_4}$) of 55.1% at a low potential of −246 mV *vs.* reversible hydrogen electrode (RHE), and the highest $FE_{C_2H_4}$ reached 60.3%. This superior electrochemical performance was attributed to the abundant coverage of *OH on the surface of the nano-sized Cu catalyst. Density functional theory (DFT) simulations revealed that the presence of *OH on the Cu catalyst surface lowers both the barriers of CO_2 activation and C–C coupling, thereby efficiently decreasing the overpotential and enhancing the selectivity for ethylene.

[a] *Key Laboratory of Interfacial Physics and Technology, Shanghai Institute of Applied Physics, Chinese Academy of Sciences, Shanghai 201800, P. R. China. E-mail: jingchao@sinap.ac.cn, wangjianqiang@sinap.ac.cn, zhanglinjuan@sinap.ac.cn*

[b] *University of Chinese Academy of Sciences, Beijing 100049, P. R. China*

[c] *Songshan Lake Materials Laboratory, Dongguan 523808, P. R. China*

† Electronic supplementary information (ESI) available. See DOI: https://doi.org/10.1039/d4cc03845b

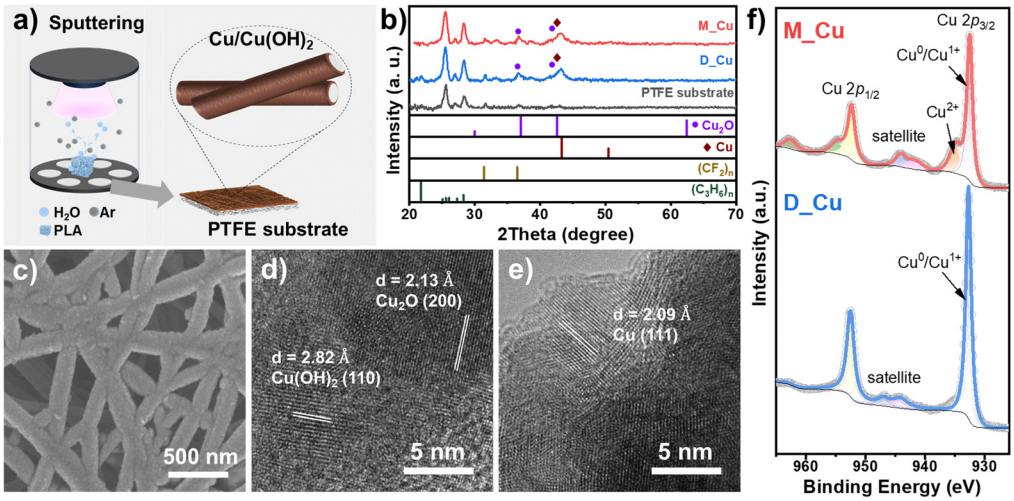

Fig. 1 (a) Schematic illustration of the method for the deposition of Cu/Cu(OH)$_2$ catalysts onto a polytetrafluoroethylene (PTFE) substrate *via* ion sputtering in a moist Ar atmosphere. (b) Grazing incidence X-ray diffraction (GI-XRD) patterns of M_Cu, D_Cu and the PTFE substrate (with $(CF_2)_n$ (JCPDS#54-1594), $(C_3H_6)_n$ (JCPDS#54-1936), Cu_2O (JCPDS#34-1354) and Cu (JCPDS#04-0836) as references). (c) Field-emission scanning electron microscopy (FESEM) image of M_Cu. (d) and (e) High-resolution transmission electron microscopy (HRTEM) of M_Cu. (f) X-ray photoelectron spectroscopy (XPS) of M_Cu and D_Cu.

The morphology of the as-prepared Cu-sputtered PTFE electrodes was characterized using field-emission scanning electron microscopy (FESEM). The ion-sputtered Cu species were coated uniformly on PTFE fibers while maintaining the porous structure, which facilitated the gas diffusion of CO_2 from the back to the Cu front (Fig. 1c and Fig. S4 and S5, ESI†). The crystalline phase of the Cu catalysts was identified using grazing incidence X-ray diffraction (GI-XRD) (Fig. 1b). Apart from the characteristic peaks of $(CF_2)_n$ and $(C_3H_6)_n$ from the polypropylene-supported PTFE membrane, M_Cu and D_Cu showed diffraction patterns matching with Cu_2O and metallic Cu. We assume that the formation of Cu_2O is due to the rapid oxidation of Cu nanoparticles upon exposure to air. From the high-resolution transmission electron microscopy (HRTEM) image in Fig. S6 (ESI†), the lattice fringes of 0.208 and 0.213 nm of D_Cu match well with the Cu (111) and Cu_2O (200), indicating the coexistence of Cu and Cu_2O, consistent with the XRD analysis. For M_Cu (Fig. 1d and e), lattice fringes with interplanar spacings of 0.209, 0.213, and 0.282 nm were observed, aligning with the Cu (111), Cu_2O (200), and (110) lattice planes of $Cu(OH)_2$, respectively. We assume that the formation of $Cu(OH)_2$ was facilitated by the introduction of H_2O molecules during the sputtering process. Elemental mapping conducted to assess the distribution of Cu along individual PTFE fibers (Fig. S7, ESI†) demonstrated the co-localization of Cu, O, C, and F in both M_Cu and D_Cu, signifying the uniform coating of sputter-deposited Cu onto the PTFE fibers. The presence of O is attributed to the oxidation of Cu in ambient air.

X-ray photoelectron spectroscopy (XPS) analysis was used to further investigate the chemical states of the surface Cu species (Fig. 1f). D_Cu showed a distinct Cu $2p_{3/2}$ peak at 932.6 eV and a weak satellite feature, corresponding to Cu^0/Cu^{1+}. It is difficult to distinguish the oxidation states of Cu^0 and Cu^{1+} using the Cu $2p_{3/2}$ peak since the binding energies of the two species are too close. For M_Cu, apart from the spark Cu^0/Cu^{1+} peak, a shoulder at a higher binding energy (934.7 eV) was clearly observed, which can be attributed to $Cu(OH)_2$.[15] In addition, the Cu $2p_{3/2}$ XPS of M_Cu showed more pronounced satellite features at a lower binding energy compared to D_Cu, supporting the presence of Cu^{2+} species. The Cu LMM Auger spectrum (Fig. S8, ESI†) showed a peak at 570.0 eV for D_Cu and at 570.4 eV for M_Cu, corresponding to Cu_2O and $Cu(OH)_2$, respectively.[15] The presence of $Cu(OH)_2$ on M_Cu was also corroborated by the OH vibrational peaks in the infrared spectra (Fig. S9, ESI†).[24]

Owing to their porous structure and the electrically conductive Cu coating, the Cu/PTFE electrodes were directly used as gas diffusion electrodes for CO_2RR measurements. As shown in Fig. 2a, the linear sweep voltammetry (LSV) curves of M_Cu exhibited a larger current density and a lower onset potential than those of D_Cu, implying higher catalytic activity of M_Cu. In addition, M_Cu showed a lower charge transfer resistance and Tafel slope (Fig. S10, ESI†) than D_Cu, indicating faster reaction kinetics. The faradaic efficiencies for each gaseous product of M_Cu and D_Cu at different current densities from −10 to −200 mA cm^{-2}, along with the corresponding potentials, are depicted in Fig. 2b and Fig. S11, S12 (ESI†). The $FE_{C_2H_4}$ of M_Cu (Fig. 2b) reached up to 60.34% at a current density of −100 mA cm^2 and achieved long-term stability for 12 h (Fig. S13, ESI†). In contrast, the optimal $FE_{C_2H_4}$ of D_Cu was only 48%. It is worth noting that both M_Cu and D_Cu exhibited better CO_2RR performance in comparison to commercial copper nanoparticles (Cu NPs; Fig. S14a, ESI†) and copper sputtered carbon paper (Fig. S14b, ESI†), demonstrating the advantage of our ion-sputtered Cu/PTFE electrodes with smaller particle size and more solid–liquid–gas three-phase interfaces.

Furthermore, M_Cu exhibits an exceptionally low overpotential, *ca.* −0.2 V, for catalyzing CO_2RR-ethylene conversion, indicating the prompt activation of CO_2 to CO and subsequent

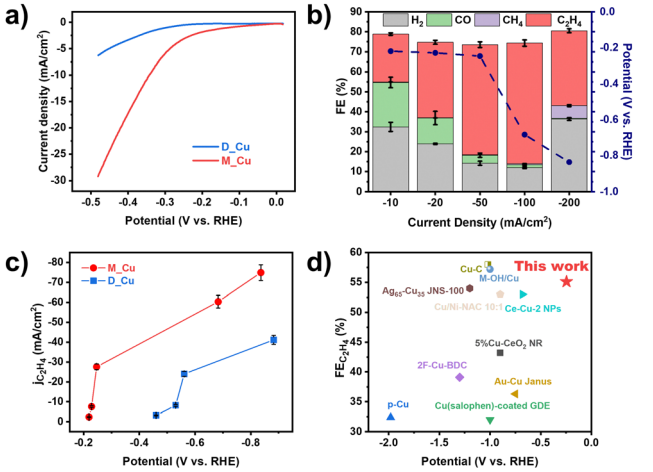

Fig. 2 (a) Linear-sweep voltammetry (LSV) curves of M_Cu and D_Cu. (b) Faradaic efficiency for each CO_2RR gaseous product of M_Cu at different current densities and the corresponding potentials. (c) Partial current density of C_2H_4 of M_Cu and D_Cu at different applied potentials. (d) Comparison of the faradaic efficiency for C_2H_4 ($FE_{C_2H_4}$) and the corresponding potentials with documented CO_2RR electrocatalysts.

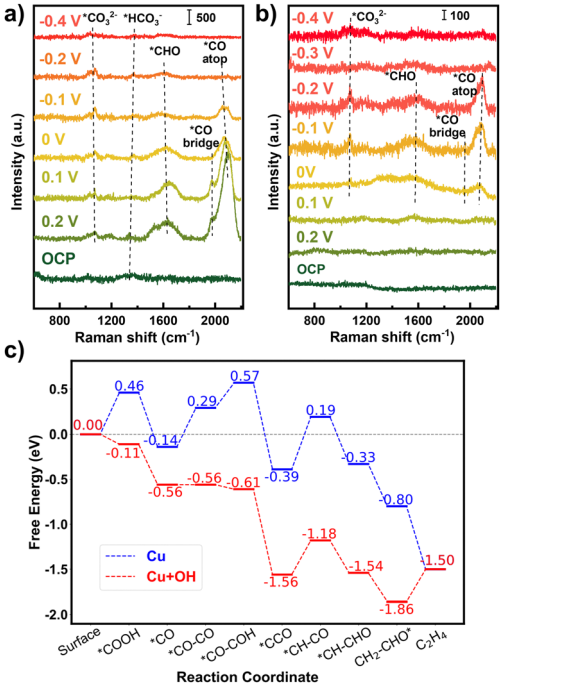

Fig. 3 *In situ* Raman spectra of (a) M_Cu and (b) D_Cu. (c) DFT calculated free energy diagram of the CO_2RR path for C_2H_4 on the Cu(111) surface with and without hydroxylation.

coupling to ethylene. Notably, the $FE_{C_2H_4}$ of M_Cu surpassed 50% when the potential reached −249 mV (Fig. 2b and Fig. S15, ESI†), demonstrating excellent performance in terms of overpotential and ethylene selectivity compared to recently reported advanced studies (Fig. 2d).[25–34] In addition, Fig. 2c compares the potential-dependent ethylene partial current density of the catalysts. M_Cu exhibited nearly double the partial current density of D_Cu and a steeper slope across the tested potential range. These findings suggest the key function of Cu–OH species in activating CO_2RR-to-ethylene at lower potentials.

In order to identify the reaction intermediates on the surface of Cu catalysts during the CO_2RR, *in situ* Raman spectroscopy was carried out under applied potentials from open circuit potential (OCP) to −0.4 V. M_Cu and D_Cu were prepared on Au electrodes instead of PTFE membranes to enhance the Raman signals. The Raman spectrum of M_Cu (Fig. 3a) showed distinct peaks at Raman shifts of 1610, 1976, and 2075 cm^{-1} upon reaching 0.2 V. These peaks are assigned to *CHO, $*CO_{bridge}$, and $*CO_{atop}$, respectively. The intensity of these peaks gradually reduced as the applied potential decreased from 0.1 V to −0.1 V, and diminished at −0.2 V, suggesting a faster CO_2RR process at lower potentials, where the intermediate products were rapidly consumed. The peak intensity of $*CO_{atop}$ is much higher than that of $*CO_{bridge}$, indicating preferential adsorption of CO at the atop site of Cu for M_Cu, which is beneficial for carbon–carbon coupling.[17] In addition, two weak peaks were observed at 1060 and 1355 cm^{-1}, corresponding to $*CO_3^{2-}$ and $*HCO_3^-$ species from the electrolyte, respectively. The *in situ* Raman spectra of D_Cu (Fig. 3b) showed three peaks at 1080, 1545, 1960, and 2070 cm^{-1} at 0 V, attributed to $*CO_3^{2-}$, *CHO, $*CO_{bridge}$ and $*CO_{atop}$ species, respectively. Comparing the Raman spectra of M_Cu and D_Cu, it is evident that M_Cu exhibited significant intermediate product peaks at a higher potential (0.2 V). This observation correlates with the electrochemical results that M_Cu displayed a lower onset potential during the CO_2RR (Fig. 2b). Additionally, M_Cu exhibited a much higher peak intensity for the intermediate products compared to D_Cu (Fig. S16, ESI†), implying higher reaction activity. Control experiments conducted on bare Au electrodes did not show observable Raman signals (Fig. S17, ESI†).

After the CO_2RR experiments, M_Cu and D_Cu were characterized using SEM. The morphology of post-reaction D_Cu was similar to its pristine structure (Fig. S18a, ESI†). Surprisingly, the post-reaction M_Cu (Fig. S18b, ESI†) showed needle-like structures, suggesting substantial restructuring of the Cu catalyst during the reaction induced by Cu–OH. In Fig. S19a (ESI†), XPS of post-reaction M_Cu exhibited a decrease in the area of the Cu^{2+} peak, indicating partial reduction of $Cu(OH)_2$ to Cu during the CO_2RR. After Ar etching (approximately 4 nm depth), as shown in Fig. S19b (ESI†), the disappearance of the Cu^{2+} peak confirmed the presence of $Cu(OH)_2$ mainly at the surface (Fig. S19a, ESI†). The XPS peaks for post-reaction D_Cu are in accordance with those in the pre-reaction state (Fig. S20a and b, ESI†), suggesting minimal changes in the catalyst.

To understand the promotional mechanism of the OH species on Cu for the CO_2RR, we calculated the CO_2RR reaction path for C_2H_4 on the Cu(111) surface employing density functional theory (DFT). The potential energy surfaces with and without hydroxylation were compared, as shown in Fig. 3c. The corresponding structures of the intermediates are listed in Fig. S21 (ESI†). For the first CO_2 activation step, the intermediate *COOH on the clean Cu surface has a relatively higher energy (0.46 eV), while an additional OH group brings its energy below

zero. This result is consistent with the *in situ* Raman spectroscopy results in Fig. 3a and b, where CO was observed much earlier (lower voltage needed) for M_Cu catalyst. After hydroxylation, the energy of *CO–CO coupling decreases from 0.43 eV to nearly 0 eV. This demonstrates a good agreement with the experimental observation that M_Cu exhibited a lower overpotential and a higher faradaic efficiency of ethylene compared to D_Cu. Furthermore, the rate-determining step (*CO–COH to *CCO) for the Cu–OH structure showed a lower energy barrier of 0.38 eV than that of bare Cu (0.58 eV), which is consistent with the low CO_2RR overpotential of M_Cu.

In summary, we present an efficient CO_2RR electrode, which is obtained by uniform dispersion of nano-sized copper particles onto a PTFE substrate using ion sputtering. The hydrophobic PTFE effectively inhibited the H_2 evolution and enhanced the solid–liquid–gas interfaces. Particularly, the surface *OH on the electrode was elegantly modulated by sputtering in a moist Ar atmosphere. The prepared M_Cu with increased surface *OH coverage achieved a $FE_{C_2H_4}$ over 50% at an exceptionally low potential of −246 mV, with an optimal ethylene faradaic efficiency of 60.3%. Through *in situ* Raman spectroscopy and DFT calculations, it has been revealed that the surface *OH species facilitate both the activation of CO_2 and the C–C coupling steps. This work demonstrates a novel strategy for the modification of Cu-based catalysts for a low-potential CO_2RR to ethylene with high activity and selectivity. We believe our findings deepen the comprehension of CO_2 electroreduction mechanisms and contribute valuable insights for the efficient design of catalysts.

The manuscript was written through contributions of all authors. All authors have given approval to the final version of the manuscript.

This work was supported by the Strategic Priority Research Program of the Chinese Academy of Sciences (grant no. XDA0400000), the National Natural Science Foundation of China (grant no. 22179141 and 22309199), the Youth Innovation Promotion Association Chinese Academy of Sciences (2023270), the Talent Plan of Shanghai Branch, Chinese Academy of Sciences (CASSHB-QNPD-2023-006), and the Photon Science Center for Carbon Neutrality.

Data availability

The data supporting this article have been included as part of the ESI.†

Conflicts of interest

There are no conflicts to declare.

Notes and references

1 P. De Luna, C. Hahn, D. Higgins, S. A. Jaffer, T. F. Jaramillo and E. H. Sargent, *Science*, 2019, **364**, eaav3506.
2 O. S. Bushuyev, P. De Luna, C. T. Dinh, L. Tao, G. Saur, J. van de Lagemaat, S. O. Kelley and E. H. Sargent, *Joule*, 2018, **2**, 825–832.
3 Y. Y. Birdja, E. Pérez-Gallent, M. C. Figueiredo, A. J. Göttle, F. Calle-Vallejo and M. T. M. Koper, *Nat. Energy*, 2019, **4**, 732–745.
4 C. Zhan, F. Dattila, C. Rettenmaier, A. Bergmann, S. Kühl, R. García-Muelas, N. López and B. R. Cuenya, *ACS Catal.*, 2021, **11**, 7694–7701.
5 H. F. Li, T. F. Liu, P. F. Wei, L. Lin, D. F. Gao, G. X. Wang and X. H. Bao, *Angew. Chem., Int. Ed.*, 2021, **60**, 14329–14333.
6 C. Choi, S. Kwon, T. Cheng, M. J. Xu, P. Tieu, C. Lee, J. Cai, H. M. Lee, X. Q. Pan, X. F. Duan, W. A. Goddard and Y. Huang, *Nat. Catal.*, 2020, **3**, 804–812.
7 A. Bagger, W. Ju, A. S. Varela, P. Strasser and J. Rossmeisl, *ChemPhysChem*, 2017, **18**, 3266–3273.
8 K. Tran and Z. W. Ulissi, *Nat. Catal.*, 2018, **1**, 696–703.
9 C. T. Dinh, T. Burdyny, M. G. Kibria, A. Seifitokaldani, C. M. Gabardo, F. P. G. de Arquer, A. Kiani, J. P. Edwards, P. De Luna, O. S. Bushuyev, C. Q. Zou, R. Quintero-Bermudez, Y. J. Pang, D. Sinton and E. H. Sargent, *Science*, 2018, **360**, 783–787.
10 J. Huang, J. W. Dai, J. N. Zhu, R. Chen, X. Q. Fu, H. F. Liu and G. F. Li, *J. Catal.*, 2022, **415**, 134–141.
11 J. Zhang, Z. P. Liu, H. S. Guo, H. R. Lin, H. Wang, X. Liang, H. L. Hu, Q. B. Xia, X. X. Zou and X. X. Huang, *ACS Appl. Mater. Interfaces*, 2022, **14**, 19388–19396.
12 S. H. Chen, C. L. Ye, Z. W. Wang, P. Li, W. J. Jiang, Z. C. Zhuang, J. X. Zhu, X. B. Zheng, S. Zaman, H. H. Ou, L. Lv, L. Tan, Y. Q. Su, J. Ouyang and D. S. Wang, *Angew. Chem., Int. Ed.*, 2023, **62**, e202315621.
13 M. Dhiman, Y. Y. Chen, Y. F. Li, A. B. Laursen, K. U. D. Calvinho, T. G. Deutsch and G. C. Dismukes, *J. Mater. Chem. A*, 2023, **11**, 717–725.
14 H. Li, W. Fang, L. X. Wang, Y. Liu, L. Liu, T. Sun, C. Liao, Y. Zhu, L. Wang and F. S. Xiao, *Innovation*, 2023, **4**, 100445.
15 S. Y. Lee, H. Jung, N.-K. Kim, H.-S. Oh, B. K. Min and Y. J. Hwang, *J. Am. Chem. Soc.*, 2018, **140**, 8681–8689.
16 S. Mu, H. Lu, Q. Wu, L. Li, R. Zhao, C. Long and C. Cui, *Nat. Commun.*, 2022, **13**, 3694.
17 G. Iijima, T. Inomata, H. Yamaguchi, M. Ito and H. Masuda, *ACS Catal.*, 2019, **9**, 6305–6319.
18 M. X. Sun, A. Staykov and M. Yamauchi, *ACS Catal.*, 2022, **12**, 14856–14863.
19 M. Li, T. Li, C. Sun, Y. Li, P. Wan, J. Qin, R. Gao, Y. Lv and Y. Song, *Mater. Today Energy*, 2024, **42**, 101568.
20 T.-K. Cheng, N. Jeromiyas, Y.-K. Lin, C.-C. Yang, C.-L. Kao, P.-Y. Chen and C.-L. Lee, *Appl. Surf. Sci.*, 2024, **660**, 159978.
21 Z. Xing, L. Hu, D. S. Ripatti, X. Hu and X. Feng, *Nat. Commun.*, 2021, **12**, 136.
22 H. Liu, C. H. Yang, T. Bian, H. J. Yu, Y. M. Zhou and Y. W. Zhang, *Angew. Chem., Int. Ed.*, 2024, **63**, e202404123.
23 X. B. Xu, D. F. Xiao, Y. G. Gao, W. B. Li, M. M. Gao, S. Zhao, Z. Y. Wang, Z. K. Zheng, P. Wang, H. F. Cheng, Y. Y. Liu, Y. Dai and B. B. Huang, *ACS Appl. Mater. Interfaces*, 2024, **16**, 16243–16252.
24 B. M. Marsh, J. Zhou and E. Garand, *J. Phys. Chem. A*, 2014, **118**, 2063–2071.
25 Z. X. Gu, H. Shen, Z. Chen, Y. Y. Yang, C. Yang, Y. L. Ji, Y. H. Wang, C. Zhu, J. L. Liu, J. Li, T. K. Sham, X. Xu and G. F. Zheng, *Joule*, 2021, **5**, 429–440.
26 R. Z. Chen, L. Cheng, J. Z. Liu, Y. T. Wang, W. X. Ge, C. Q. Xiao, H. Jiang, Y. H. Li and C. Z. Li, *Small*, 2022, **18**, 2200720.
27 Y. B. Ma, J. L. Yu, M. Z. Sun, B. Chen, X. C. Zhou, C. L. Ye, Z. Q. Guan, W. H. Guo, G. Wang, S. Y. Lu, D. S. Xia, Y. H. Wang, Z. He, L. Zheng, Q. B. Yun, L. Q. Wang, J. W. Zhou, P. Y. Lu, J. W. Yin, Y. F. Zhao, Z. B. Luo, L. Zhai, L. W. Liao, Z. L. Zhu, R. Q. Ye, Y. Chen, Y. Lu, S. B. Xi, B. L. Huang, C. S. Lee and Z. X. Fan, *Adv. Mater.*, 2022, **34**, 2110607.
28 J. J. Shan, Y. X. Shi, H. Y. Li, Z. Y. Chen, C. Y. Sun, Y. Shuai and Z. J. Wang, *Chem. Eng. J.*, 2022, **433**, 133769.
29 M. Sun, A. Staykov and M. Yamauchi, *ACS Catal.*, 2022, **12**, 14856–14863.
30 Z. Y. Yin, J. Q. Yu, S. W. Yu, Z. H. Xie, L. Y. Zhang, T. Akauola, J. G. G. Chen, W. Y. Huang, L. Qi and S. Zhang, *J. Am. Chem. Soc.*, 2022, **144**, 20931–20938.
31 Y. Q. Zheng, J. W. Zhang, Z. S. Ma, G. G. Zhang, H. F. Zhang, X. W. Fu, Y. Y. Ma, F. Liu, M. C. Liu and H. W. Huang, *Small*, 2022, **18**, 2201695.
32 S. Hong, H. G. Abbas, K. Jang, K. K. Patra, B. Kim, B. U. Choi, H. Song, K. S. Lee, P. P. Choi, S. Ringe and J. Oh, *Adv. Mater.*, 2023, **35**, 2208996.
33 S. Wang, J. L. Zhang, L. Yao, Y. S. Yang, L. R. Zheng, B. Guan, Y. Z. Zhao, Y. Y. Wang, B. X. Han and X. Q. Xing, *Nano Res.*, 2023, **16**, 10779–10786.
34 L. J. Zhu, D. H. Si, F. X. Ma, M. J. Sun, T. Zhang and R. Cao, *ACS Catal.*, 2023, **13**, 5114–5121.